Aeroelastic Analysis of Wings Using the Euler Equations with a Deforming Mesh

Brian A. Robinson*
Purdue University, West Lafayette, Indiana 47907
John T. Batina†
NASA Langley Research Center, Hampton, Virginia 23665
and
Henry T. Y. Yang‡
Purdue University, West Lafayette, Indiana 47907

Modifications to the CFL3D three-dimensional unsteady Euler/Navier-Stokes code for the aeroelastic analysis of wings are described. The modifications involve including a deforming mesh capability that can move the mesh to continuously conform to the instantaneous shape of the aeroelastically deforming wing and also including the structural equations of motion for their simultaneous time integration with the governing flow equations. Calculations were performed using the Euler equations to verify the modifications to the code and as a first step toward aeroelastic analysis using the Navier-Stokes equations. Results are presented for the NACA 0012 airfoil and a 45-deg sweptback wing to demonstrate applications of CFL3D for generalized force computations and aeroelastic analysis. Comparisons are made with published Euler results for the NACA 0012 airfoil and with experimental flutter data for the 45-deg sweptback wing to access the accuracy of the present capability. These comparisons show good agreement and, thus, the CFL3D code may be used with confidence for aeroelastic analysis of wings. The paper describes the modifications that were made to the code and presents results and comparisons that assess the capability.

Nomenclature

A_{ij} = generalized aerodynamic force resulting from pressure induced by mode j acting through mode i
a = nondimensional distance from midchord to elastic axis
a_∞ = freestream speed of sound
b = semichord, $c/2$
C_p = pressure coefficient
c = reference chord
c_i = generalized damping of mode i
k = reduced frequency, $\omega c/2U_\infty$
k_i = generalized stiffness of mode i
M_∞ = freestream Mach number
m = airfoil mass per unit span
m_i = generalized mass of mode i
Q = dynamic pressure, $\frac{1}{2}\rho_\infty U_\infty^2$
$\bar{Q}$ = nondimensional dynamic pressure, $[U_\infty/b\omega_\alpha\sqrt{\mu}]^2$
Q_i = generalized force in mode i
q_i = generalized displacement of mode i
r_α = airfoil radius of gyration about elastic axis
T = time, s
t = time, nondimensionalized by freestream speed of sound and airfoil chord, Ta_∞/c
U_∞ = streamwise freestream speed
u_i = load vector
x_i = state vector
x_α = nondimensional distance from elastic axis to mass center
α_0 = mean angle of attack
Θ = integral of state-transition matrix
μ = mass ratio
ρ_∞ = freestream density
σ = real part of Laplace transform variable
Φ = state-transition matrix
ω = angular frequency
ω_h = uncoupled natural frequency of bending mode
ω_α = uncoupled natural frequency of torsion mode

Received Dec. 19, 1989; presented as Paper 90-1032 at the AIAA/ASME/ASCE/AHS/ASC 31st Structures, Structural Dynamics, and Materials Conference, Long Beach, CA, April 2-4, 1990; revision received Oct. 1, 1990; accepted for publication Nov. 9, 1990.

*Graduate Research Assistant, School of Aeronautics and Astronautics; currently Engineer/Technology, McDonnell Aircraft Co., St. Louis, MO 63166. Member AIAA.

†Research Scientist, Unsteady Aerodynamics Branch, Structural Dynamics Division. Senior Member AIAA.

‡Professor and Dean, Schools of Engineering. Fellow AIAA.

Introduction

In recent years, there has been increased interest in the development of aeroelastic analysis methods involving computational fluid dynamics techniques.[1] This research has been highly focused on developing finite difference codes for the solution of the transonic small-disturbance[2,3] and full potential[4,5] equations, although efforts are currently underway at the higher equation levels as well.[6-11] For example, Bendiksen and Kousen[6] presented transonic flutter results for two-degree-of-freedom (plunging and pitching) airfoils by simultaneously integrating the structural equations of motion with the two-dimensional unsteady Euler equations. The Euler equations were integrated using a Runge-Kutta time-stepping scheme involving a finite-volume spatial discretization and a moving mesh. The instantaneous mesh was taken to be a linear combination of meshes corresponding to rigid plunging and pitching of the airfoil. In a following study, Kousen and Bendiksen[7] applied their method of Ref. 6 to investigate the nonlinear aeroelastic behavior of two-degree-of-freedom airfoils at transonic speeds. In Ref. 7, transonic flutter instabilities were shown to lead to stable limit-cycle oscillations. Wu et al.[8] have time-integrated the unsteady compressible Navier-Stokes

equations for airfoils undergoing one- and two-degree-of-freedom aeroelastic motions. In Ref. 8, flutter characteristics of airfoils at high angles of attack were investigated, including cases with stall flutter. The method of Ref. 8 has also been recently applied by Reddy et al.[9] to study the effects of rotational flow, viscosity, thickness, and shape on the transonic flutter dip phenomena. The study concluded that the influence of these effects on flutter, for the cases considered, was small near the minimum of the flutter dip, but may be large away from the dip. Guruswamy[10] has demonstrated the simultaneous time integration of the three-dimensional Euler equations along with the structural equations of motion. The capability was demonstrated in a time-marching flutter analysis performed for a rectangular wing with a parabolic-arc airfoil section. Finally, Rausch et al.[11] have presented Euler aeroelastic results for two-degree-of-freedom airfoils using a flow solver based on unstructured grids. A novel aspect of the capability of Ref. 11 is the dynamic mesh algorithm used to move the mesh so that it continuously conforms to the instantaneous position of the airfoil. The algorithm is completely general in that it can treat realistic motions and deformations of multiple two-dimensional bodies.

Many of the methods that are currently being developed for aeroelastic analysis assume that the mesh moves rigidly or that the mesh shears as the body deforms. These assumptions consequently limit the applicability of the procedures to rigid-body or small-amplitude motions. These problems, for example, are easily demonstrated by considering an airfoil section of a wing whose aeroelastic deformation involves significant chordwise bending. As the airfoil section bends, grid lines that emanate from the concave surface of the section may collapse onto the neighboring grid lines. Similar difficulties can occur if the wing has significant spanwise bending. Also, for methods where the mesh is constrained, such that airfoil sections of the wing can only pitch and plunge, chordwise deformation cannot be modeled and wing tip deflections must remain small. The purpose of this paper, therefore, is to describe the implementation of a deforming mesh capability that effectively removes the rigid-body and small-amplitude limitations of previous methods. This capability was developed within the CFL3D unsteady Euler/Navier-Stokes code.[12,13] The deforming mesh capability is a general procedure, based on the dynamic mesh algorithm of Refs. 11 and 14, which can move the mesh for realistic motions and structural deformations of wings. In addition, the structural equations of motion have been implemented within CFL3D to allow simultaneous time integration with the governing flow equations for aeroelastic analysis. Calculations were performed using the Euler equations to verify the modifications to the code, and as a first step toward aeroelastic analysis using the Navier-Stokes equations. Results are presented for the NACA 0012 airfoil and a 45-deg sweptback wing to demonstrate applications of CFL3D for generalized force computation and aeroelastic analysis. Comparisons are made with the Euler results of Ref. 11 for the NACA 0012 airfoil and with the experimental flutter data of Ref. 15 for the 45-deg sweptback wing to assess the accuracy of the present procedures. This paper describes the modifications that were made to the CFL3D code and presents results and comparisons that assess the capability.

Euler Solution Algorithm

In the present study, the flow was assumed to be governed by the time-dependent Euler equations, which may be written in conservation form as

$$\frac{\partial \hat{Q}}{\partial t} + \frac{\partial \hat{F}}{\partial \xi} + \frac{\partial \hat{G}}{\partial \eta} + \frac{\partial \hat{H}}{\partial \zeta} = 0 \tag{1}$$

where the vector $\hat{Q}$ represents the conserved variables divided by the Jacobian, and $\hat{F}$, $\hat{G}$, and $\hat{H}$ are the inviscid fluxes that have been transformed from the Cartesian (x,y,z) coordinate system to generalized (ξ,η,ζ) coordinates. Equation (1) is solved within the CFL3D code by a three-factor implicit finite-volume algorithm based on upwind-biased spatial differencing. The upwind-biased differencing involves either flux-vector splitting or flux-difference splitting implemented as a cell-centered discretization. Flux limiting may also be used in the spatial differencing to determine values of the flow variables on the cell faces. For unsteady applications, the algorithm includes the grid speed metric terms that are necessary for time accuracy with moving meshes, although the original scheme was limited to cases involving rigid-body plunge or pitch, where the mesh moves without deformation. Modifications to the algorithm to include the terms arising from a deforming mesh, which are required for aeroelastic analysis, are described in the following section.

Deforming Mesh Algorithm

A deforming mesh algorithm was developed and implemented to move the mesh so that it continuously conforms to the instantaneous shape of the aeroelastically deforming wing. The method, based on that of Ref. 14, models the mesh as a spring network, where each edge of each hexahedral cell represents a linear spring. The stiffness of each spring is inversely proportional to a specified power of the length of the edge. For example, along an edge $(i)-(i+1)$, the stiffness $k_{i+\frac{1}{2}}$ is

$$k_{i+\frac{1}{2}} = 1.0/\left[(x_{i+1}-x_i)^2+(y_{i+1}-y_i)^2+(z_{i+1}-z_i)^2\right]^{p/2} \tag{2}$$

In addition to the cell edges, springs are also placed along the diagonals of each cell face to control cell shearing, with spring stiffness defined similar to Eq. (2). The power p appearing in Eq. (2) is used to control the stiffness of the cells near the wing. These cells are typically very small in comparison with cells in the far field, and as such it has been found advantageous to increase the stiffness of the near-field cells to avoid excessive mesh distortion in this region. The stiffness is increased by increasing the value of p. In this study, p was typically set equal to two or three.

The procedure to move the mesh is described as follows. At each time step, the instantaneous positions of the points on the wing are prescribed, whereas the points on the outer boundary are held fixed. The displacements of the interior points $\delta_x, \delta_y, \delta_z$ are determined by solving the static equilibrium equations resulting from a summation of forces at each point in the x, y, and z directions. This solution is approximated by using a predictor-corrector procedure that first predicts the displacements of the interior points by a linear extrapolation of displacements from the two previous time levels, according to

$$\tilde{\delta}_{x_{i,j,k}} = 2\delta^n_{x_{i,j,k}} - \delta^{n-1}_{x_{i,j,k}} \tag{3a}$$

$$\tilde{\delta}_{y_{i,j,k}} = 2\delta^n_{y_{i,j,k}} - \delta^{n-1}_{y_{i,j,k}} \tag{3b}$$

$$\tilde{\delta}_{z_{i,j,k}} = 2\delta^n_{z_{i,j,k}} - \delta^{n-1}_{z_{i,j,k}} \tag{3c}$$

and then corrects the displacements using several Jacobi iterations of the static equations written as

$$\delta^{n+1}_{x_{i,j,k}} = \frac{k_{i+\frac{1}{2},j,k}\tilde{\delta}_{x_{i,j,k}} + \cdots + k_{i,j,k-\frac{1}{2}}\tilde{\delta}_{x_{i,j,k-1}}}{k_{i+\frac{1}{2},j,k} + \cdots + k_{i,j,k-\frac{1}{2}}} \tag{4a}$$

$$\delta^{n+1}_{y_{i,j,k}} = \frac{k_{i+\frac{1}{2},j,k}\tilde{\delta}_{y_{i,j,k}} + \cdots + k_{i,j,k-\frac{1}{2}}\tilde{\delta}_{x_{i,j,k-1}}}{k_{i+\frac{1}{2},j,k} + \cdots + k_{i,j,k-\frac{1}{2}}} \tag{4b}$$

$$\delta^{n+1}_{z_{i,j,k}} = \frac{k_{i+\frac{1}{2},j,k}\tilde{\delta}_{z_{i,j,k}} + \cdots + k_{i,j,k-\frac{1}{2}}\tilde{\delta}_{x_{i,j,k-1}}}{k_{i+\frac{1}{2},j,k} + \cdots + k_{i,j,k-\frac{1}{2}}} \tag{4c}$$

For the applications performed in the present study, two to four Jacobi iterations were sufficient to accurately move the mesh.

To demonstrate mesh movement using the deforming mesh algorithm, consider the coarse grid about a NACA 0012 air-

foil that is shown in Fig. 1a. The grid is of C-type mesh topology, and has 43 points in the "wrap-around" direction and 11 points in the outward direction. It is used only to illustrate how the mesh moves. In this example, the airfoil was plunged for one cycle of sinusoidal motion with an amplitude of one chordlength. The mesh at the maximum plunge displacement is shown in Fig. 1b, the mesh at the minimum plunge displacement in Fig. 1c. The mesh moves smoothly as the airfoil plunges, and the procedure is completely general in that it can treat realistic airfoil or wing motions, including aeroelastic transient-type motion.

Since the mesh can now deform to accommodate the aeroelastically deforming wing, the flow solver in the CFL3D code was modified to include an extra term in the time discretization of the governing equations, to account for the mesh deformation. Specifically, the modification involves the change in cell volume when the mesh deforms. The algorithm changes are derived by first writing $\partial\hat{Q}/\partial t$ in the governing equation (1) as $\partial(QV)/\partial t$, where V is the cell volume. The original flow solver assumed that the cell volume does not change in time, so that

$$\frac{\partial(QV)}{\partial t} = V\frac{\partial Q}{\partial t} \tag{5a}$$

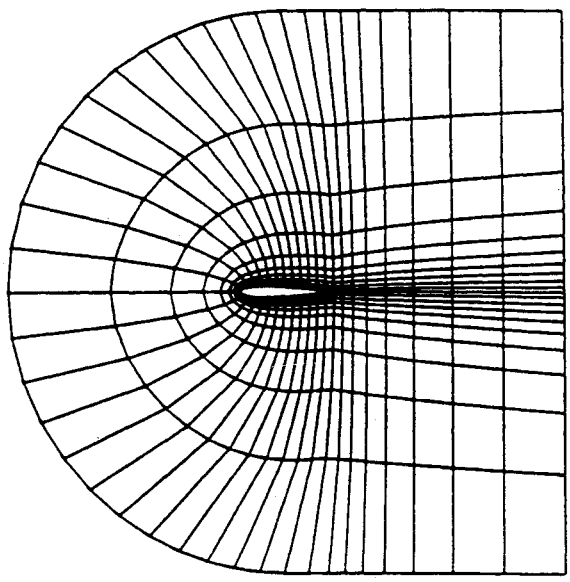

a) Original grid (for reference)

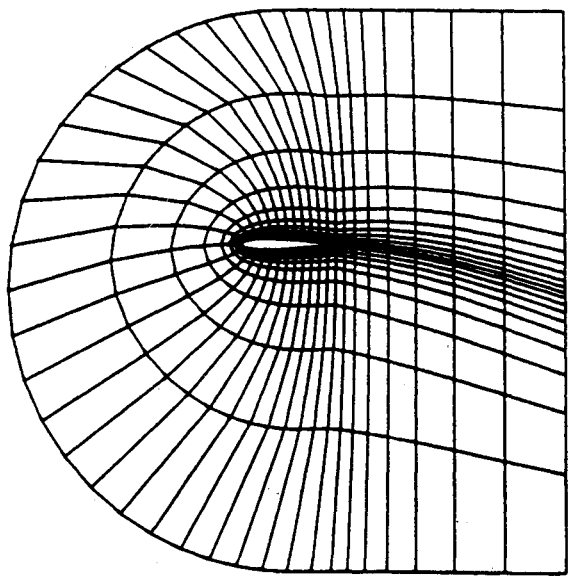

b) Plunge upward one chordlength

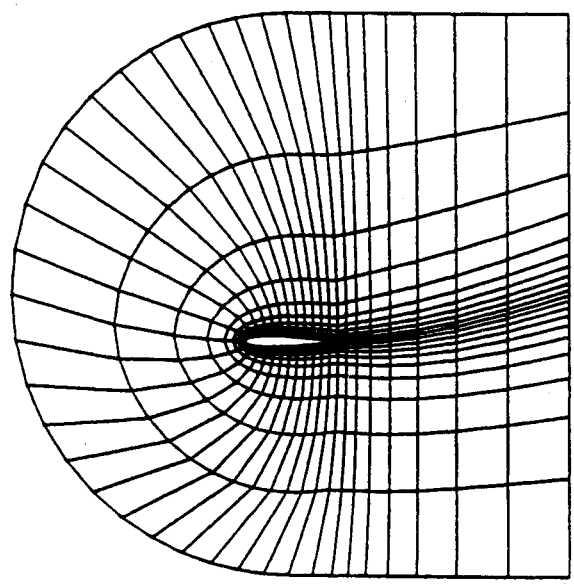

c) Plunge downward one chordlength

Fig. 1 Sequence of grids about the NACA 0012 airfoil that illustrates how the mesh moves for a plunging airfoil.

However, if the cell volume changes in time, as it does when the mesh deforms, the time derivative becomes

$$\frac{\partial(QV)}{\partial t} = V\frac{\partial Q}{\partial t} + Q\frac{\partial V}{\partial t} \tag{5b}$$

which requires the implementation of the $Q\partial V/\partial t$ term within the CFL3D algorithm.

Pulse Transfer-Function Analysis

Generalized aerodynamic forces that are used in aeroelastic analyses are typically obtained by calculating several cycles of a harmonically forced oscillation, with the determination of the forces based on the last cycle of motion. This method of harmonic oscillation requires one flow calculation for each value of reduced frequency that is of interest. In contrast, the generalized forces may be determined for a wide range of reduced frequency in a single flow calculation by the pulse transfer-function analysis. In the pulse analysis, the forces are computed indirectly from the response of the flowfield, due to an exponentially shaped pulse. The analysis assumes that the system is linear, which is a reasonable assumption even for transonic cases, since experience has shown that the response for harmonic or aeroelastic motion is, in general, locally linear for small amplitudes of oscillation.

Time-Marching Aeroelastic Analysis

In this section, the aeroelastic equations of motion, the time-marching solution procedure, and the modal identification technique are described.

Aeroelastic Equations of Motion

The aeroelastic equations of motion that were incorporated within CFL3D were derived by assuming that the general motion of the wing is described by a separation of time and space variables in a finite modal series.[16] This modal series involves the summation of free vibration modes weighted by generalized displacements. Considering Lagrange's equations leads to the equations of motion that can be written for each mode i as

$$m_i\ddot{q}_i + c_i\dot{q}_i + k_iq_i = Q_i \tag{6}$$

where q_i is the generalized normal mode displacement, m_i is the generalized mass, c_i is the generalized damping, k_i is the generalized stiffness, and Q_i is the generalized force computed by integrating the pressure weighted by the mode shapes.

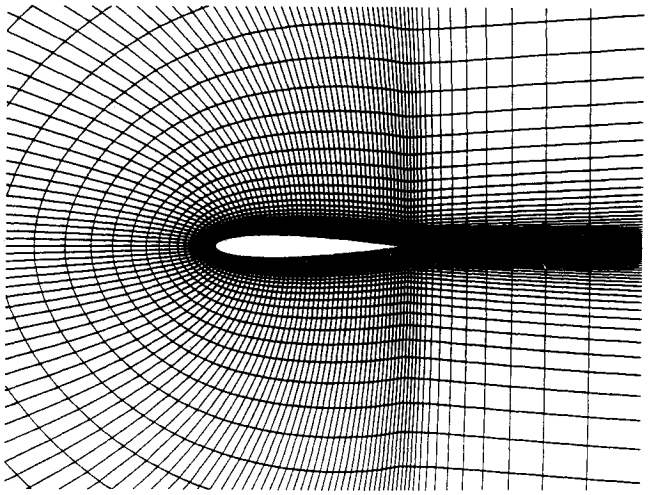

Fig. 2 Partial view of 159×49 C-type mesh about the NACA 0012 airfoil.

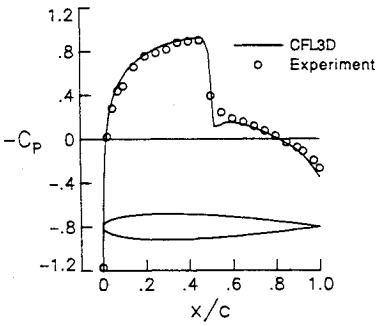

Fig. 3 Comparison of upper surface steady pressure distributions on the NACA 0012 airfoil at $M_\infty = 0.8$ and $\alpha_0 = 0$ deg.

Time-Marching Solution

The aeroelastic equations of motion are integrated in time in a manner similar to that described by Edwards et al.[17,18] The formulation is implemented herein for multiple degrees-of-freedom or mode shapes of a wing, following Ref. 16. Each normal mode equation represented by Eq. (6) can be expressed in state-space form as

$$\dot{x}_i = Ax_i + Bu_i \tag{7}$$

where A and B are coefficient matrices that result from the change of variables $x_i = [q_i \dot{q}_i]^T$, and u_i is the nondimensional generalized force weighted by mode i. Equation (7) is integrated in time using the modified state-transition matrix structural integrator[18] implemented as a predictor-corrector procedure, which first uses a linear extrapolation of u_i from previous time steps as

$$\tilde{x}_i^{n+1} = \Phi x_i^n + \Theta B(3u_i^n - u_i^{n-1})/2 \tag{8a}$$

to compute $\tilde{x}_i^{n+1}$, the prediction for x_i^{n+1}. Then, $\tilde{x}_i^{n+1}$ is used to compute the flowfield and evaluate the load vector $\tilde{u}_i^{n+1}$. These values are then used in the corrector step to determine x_i^{n+1}, given by

$$x_i^{n+1} = \Phi x_i^n + \Theta B(\tilde{u}_i^{n+1} + u_i^n)/2 \tag{8b}$$

In Eqs. (8a) and (8b), Φ is the state-transition matrix and Θ is the integral of the state-transition matrix from time step n to $n+1$.

Modal Identification Technique

Damping and frequency characteristics of the aeroelastic responses are estimated from the response curves by using the modal identification technique of Bennett and Desmarais.[19] The modal estimates are determined by a least-squares curve fit of the response of the form

$$q_i(T) = a_0 + \sum_{j=1}^{m} e^{\sigma_j T}\left[a_j \cos(\omega_j T) + b_j \sin(\omega_j T)\right] \qquad i = 1,2,\ldots \tag{9}$$

where m is the number of modes.

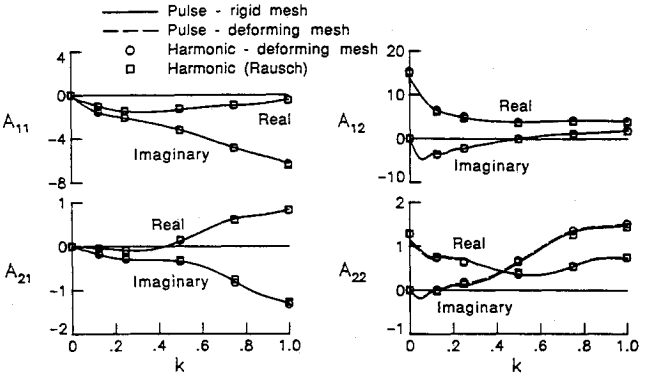

Fig. 4 Comparisons of generalized aerodynamic forces for the NACA 0012 airfoil at $M_\infty = 0.8$ and $\alpha_0 = 0$ deg.

Results and Discussion

Results are presented in this section for the NACA 0012 airfoil and a 45-deg sweptback wing, computed using CFL3D, to verify the deforming mesh capability and to assess the code for aeroelastic analysis. The accuracy of these results is determined by making detailed comparisons with CFL3D calculations performed using a rigidly moving mesh, published results obtained using alternative computational methods, and available experimental data.

NACA 0012 Airfoil Results

Calculations were performed for the NACA 0012 airfoil by using the CFL3D code run in a two-dimensional mode. The results were obtained using a 159×49 C-type mesh, a partial view of which is shown in Fig. 2. The outer boundaries of the mesh were located approximately 15 chordlengths from the airfoil and there are 110 points that lie on the airfoil surface. Calculations were performed for the airfoil at $M_\infty = 0.8$ and 0-deg angle of attack. In these calculations, the Euler equations were solved using the CFL3D code with a third-order accurate upwind-biased spatial discretization and flux-vector splitting. Steady results are compared with the experimental pressure data of Ref. 20 and the unsteady results are compared with the parallel computational results of Ref. 11, obtained using the two-dimensional Euler code of Ref. 21.

Steady Pressure Comparisons

The calculated steady pressure distribution along the upper surface of the airfoil is compared with the experimental data in Fig. 3. These pressures indicate that there is a moderately strong shock wave near the airfoil midchord, which is accurately predicted by CFL3D in both strength and location. Such a good comparison suggests that viscous effects for this case are relatively small and, thus, the flow can be modeled accurately by the Euler equations.

Generalized Force Comparisons

Generalized aerodynamic forces for the NACA 0012 airfoil are presented in Fig. 4. The results are plotted as real and imaginary components of the unsteady forces A_{ij}, as a function of reduced frequency k. Both plunge and pitch-about-the-quarter-chord motions were considered, defined as modes 1 and 2, respectively. Thus, for example, A_{12} is the lift coeffi-

cient due to pitching. Figure 4 compares results obtained using several different methods, including 1) the pulse analysis with a rigidly moving mesh, 2) the pulse analysis with a deforming mesh, 3) harmonic motion with a deforming mesh, and 4) the harmonic Euler results from Ref. 11. With the rigidly moving mesh, the mesh simply translates for airfoil plunge motion and rotates for airfoil pitch motion. The harmonic results were obtained at six values of reduced frequency: $k = 0.0$, 0.125, 0.25, 0.5, 0.75, and 1.0. The amplitudes of motion were 0.01 chordlengths and 0.1 deg for plunge and pitch, respectively, in both harmonic and pulse analyses.

As shown in Fig. 4, the forces from the pulse analysis obtained using the deforming mesh agree very well with the forces obtained using the rigidly moving mesh. This good agreement between the two sets of forces tends to verify the deforming mesh capability that was implemented within CFL3D. As further shown in Fig. 4, the pulse results agree well with the forces from the harmonic analysis, for both plunge and pitch motions, for the entire range of reduced frequency that was considered. The harmonic analysis, however, is considered to be the more accurate of the two sets of calculations, since the local linearity assumption in the pulse analysis is questionable for transonic cases. Furthermore, the generalized forces determined using the harmonic analysis agree well with the Euler forces of Rausch et al.,[11] which gives additional confidence in the accuracy of the deforming mesh capability that was implemented.

Aeroelastic Comparisons

Aeroelastic results are presented for a much-studied case, designated as Case A of Isogai,[22] which has normal modes similar to those of a streamwise section near the tip of a swept-back wing. The wind-off bending and torsion natural frequencies are 71.33 and 535.65 rad/s, respectively. The pivot point for the bending mode is located 1.44 chordlengths upstream of the leading edge of the airfoil. The pivot point for the torsion mode is 0.068 chordlengths forward of midchord. These mode shapes and natural frequencies were determined by performing a free vibration analysis with the aeroelastic equations written in the traditional form of plunge and pitch degrees of freedom. In this analysis, the following structural parameter values were used: $a = -2.0$, $x_\alpha = 1.8$, $r_\alpha = 1.865$, $\omega_h = 100$ rad/s, and $\omega_\alpha = 100$ rad/s. Also, the airfoil mass ratio was $\mu = 60$. Generalized displacements corresponding to the bending and torsion modes are defined as q_1 and q_2, respectively. Initial conditions for the time-marching aeroelastic analysis were $\dot{q}_1(0) = 2.0$ and $\dot{q}_2(0) = 0.01$.

Aeroelastic results for Case A were obtained for several values of nondimensional dynamic pressure, including $\bar{Q} = 0.2$, 0.3, 0.4, 0.5, 0.6, 0.7, and 0.8, to obtain conditions bracketing the flutter point. Figure 5 shows time responses of generalized displacement of the second coupled mode for $\bar{Q} = 0.2$, 0.5, and 0.8, which correspond to stable, near neutrally stable, and unstable aeroelastic behavior, respectively. Also plotted are the corresponding responses reported in Ref. 11. A comparison of these responses indicates that the time-marching aeroelastic results from the CFL3D code agree well with those from the Euler code of Ref. 11, which tends to verify the aeroelastic modeling procedures implemented. Shown in Fig. 6 are the two-mode curve fits of the CFL3D responses, which are excellent approximations to the original data. The component modes from these curve fits are shown in Fig. 7 for the three values of $\bar{Q}$ that were considered in Figs. 5 and 6. The results of Fig. 7 show that the component modes consist of a dominant mode corresponding to bending (mode 1) and a second higher-frequency mode corresponding to torsion (mode 2). Damping and frequency estimates from this analysis are compared with similar values from Rausch et al.[11] in Table 1. These comparisons indicate that the CFL3D values correlate well with the Euler values from Ref. 11. Also,

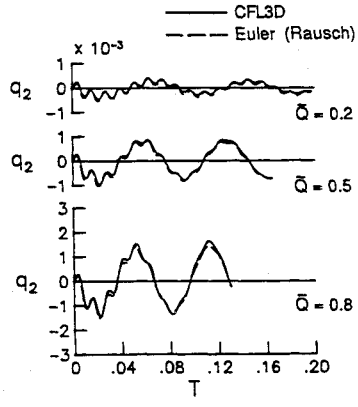

Fig. 5 Comparisons of generalized displacements for the NACA 0012 airfoil at $M_\infty = 0.8$ and $\alpha_0 = 0$ deg for Case A.

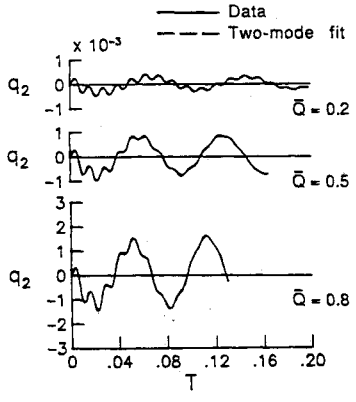

Fig. 6 Effects of nondimensional dynamic pressure on the generalized displacement of the second coupled mode for the NACA 0012 airfoil at $M_\infty = 0.8$ and $\alpha_0 = 0$ deg for Case A.

Table 1 Comparisons between aeroelastic solutions for the NACA 0012 airfoil at $M_\infty = 0.8$ and $\alpha_0 = 0$ deg for Case A

		Mode 1		Mode 2	
$\bar{Q}$	Method	σ/ω_α	ω/ω_α	σ/ω_α	ω/ω_α
0.2	CFL3D time-marching	−0.011	0.794	−0.091	5.363
	Euler (Rausch) time-marching	−0.011	0.790	−0.068	5.353
0.5	CFL3D time-marching	0.004	0.914	−0.185	5.347
	Euler (Rausch) time-marching	0.000	0.913	−0.148	5.349
0.8	CFL3D time-marching	0.026	1.027	−0.173	5.270
	Euler (Rausch) time-marching	0.017	1.022	−0.223	5.317

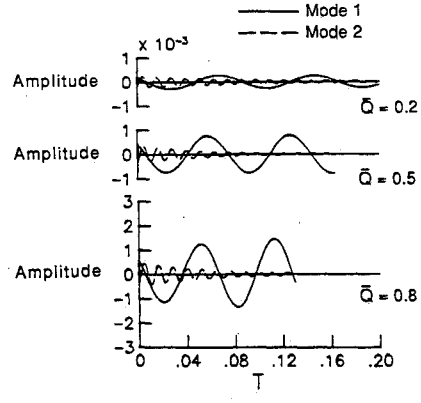

Fig. 7 Effects of nondimensional dynamic pressure on the component modes of the aeroelastic system for the NACA 0012 airfoil at $M_\infty = 0.8$ and $\alpha_0 = 0$ deg for Case A.

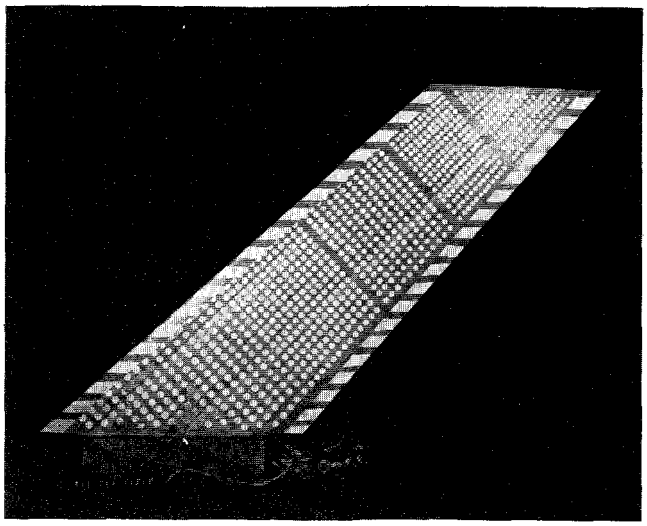

Fig. 8 Planview of 45-deg sweptback wing.

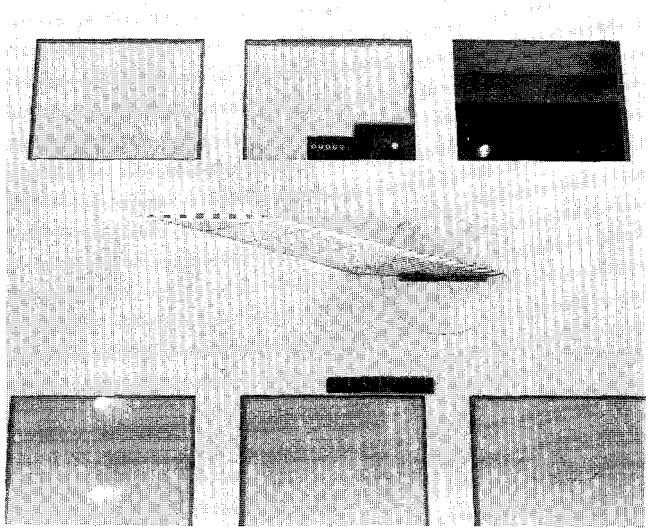

Fig. 9 45-deg sweptback wing in the NASA Langley Transonic Dynamics Tunnel.

the flutter value for $\bar{Q}$, computed by quadratic interpolation of the damping values, was 0.48 for CFL3D, which compares with 0.50, as reported in Ref. 11. Linear theory at $M_\infty = 0.8$, which, of course, does not include transonic effects, predicts a much higher flutter value of 1.89.

45-Deg Sweptback Wing Results

Calculations were performed for a simple well-defined wing, to assess the CFL3D code for three-dimensional aeroelastic applications. The wing that was analyzed was a semispan wind-tunnel-wall-mounted model that has a quarter-chord sweep angle of 45 deg, a panel aspect ratio of 1.65, and a taper ratio of 0.66.[15] The wing is an AGARD standard aeroelastic configuration, tested in the Transonic Dynamics Tunnel (TDT) at NASA Langley Research Center. A planview of the wing is shown in Fig. 8. The wing has a NACA 65A004 airfoil section, and was constructed of laminated mahogany. In order to obtain flutter for a wide range of Mach number and density conditions in the TDT, holes were drilled through the wing to reduce its stiffness. To maintain the aerodynamic shape of the wing, the holes were filled with a rigid foam plastic. A photograph of the wing mounted in the TDT is shown in Fig. 9. The wing is modeled structurally using the first four natural vibration modes, illustrated in Figs. 10 and 11. Figure 10 shows oblique projections of the natural modes; Fig. 11 shows the

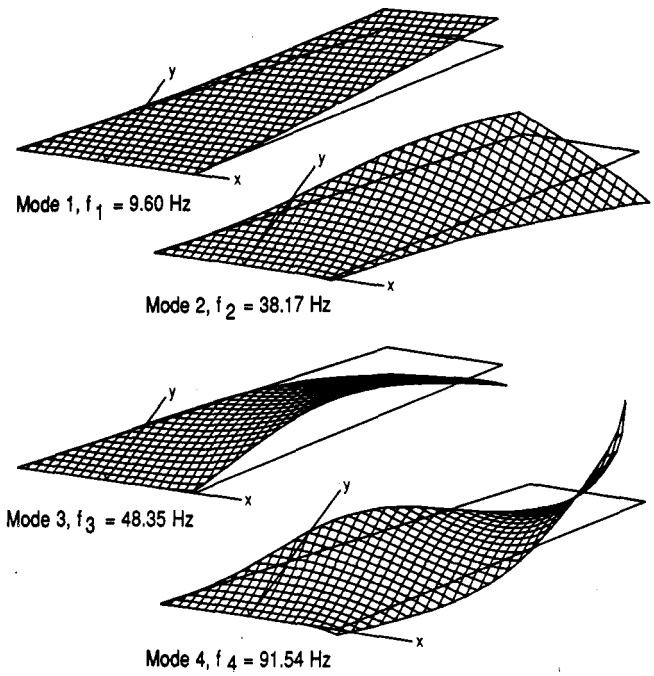

Fig. 10 Oblique projections of natural vibration modes of 45-deg sweptback wing.

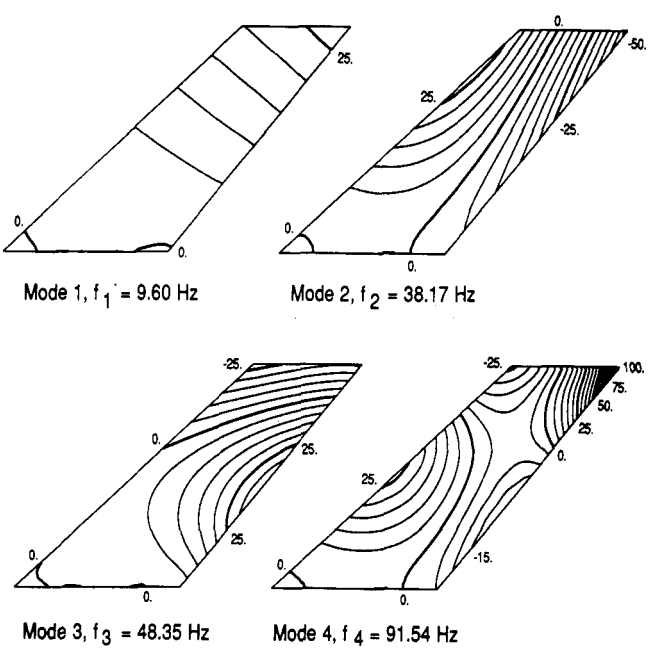

Fig. 11 Deflection contours of natural vibration modes of 45-deg sweptback wing.

corresponding deflection contours. These modes, which are numbered 1-4, represent first bending, first torsion, second bending, and second torsion, respectively, as determined by a finite element analysis. The modes have natural frequencies ranging from 9.6 Hz for the first bending mode to 91.54 Hz for the second torsion mode.

Aeroelastic results were obtained for the 45-deg sweptback wing using a $193 \times 33 \times 41$ C-H-type mesh, a partial view of which is shown in Fig. 12. Calculations were performed for the wing at $M_\infty = 0.9$ and 0-deg angle of attack. In these calculations, the Euler equations were solved using the CFL3D code with a second-order-accurate upwing-biased spatial discretization and flux-vector splitting. Aeroelastic transients were obtained for several values of dynamic pressure Q, to obtain conditions that bracket the flutter point. Figure 13 shows time responses of generalized displacement of the first bending

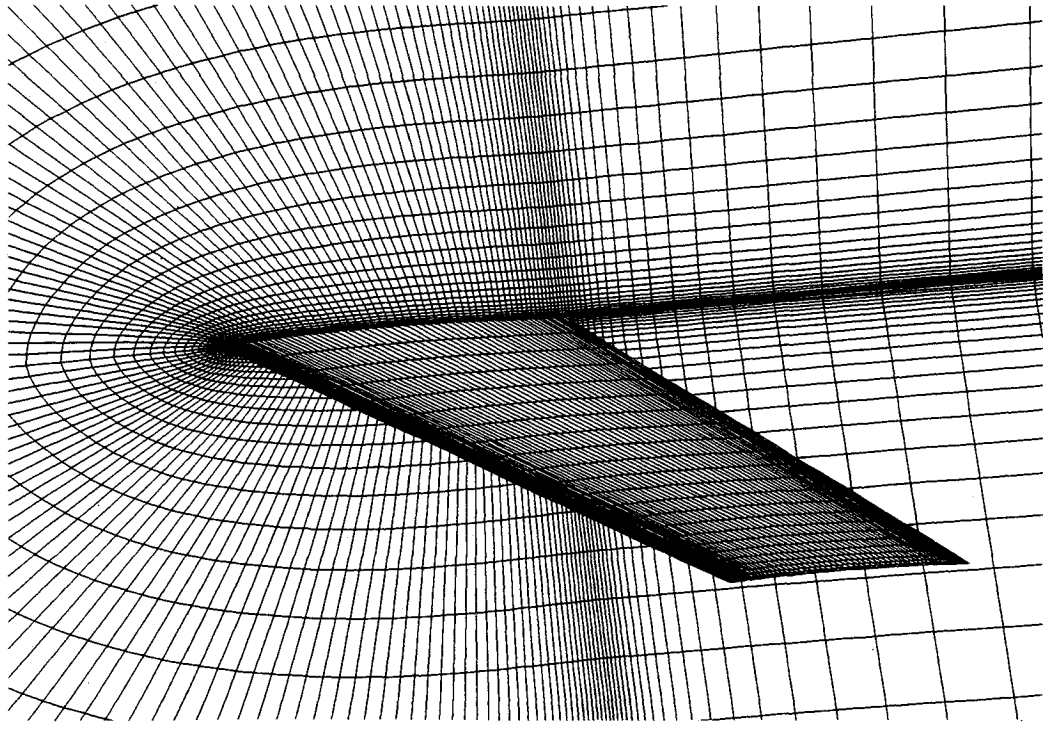

Fig. 12 Partial view of 193×33×41 C-H-type mesh about the 45-deg sweptback wing.

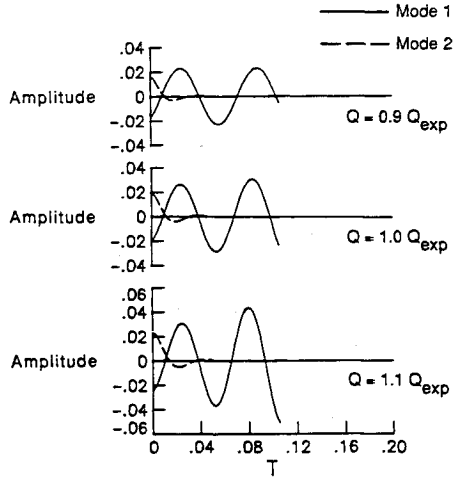

Fig. 13 Effects of dynamic pressure on the generalized displacement of the first bending mode for the 45-deg sweptback wing at $M_\infty = 0.9$ and $\alpha_0 = 0$ deg.

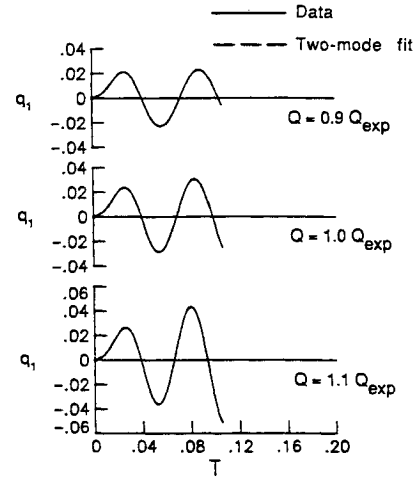

Fig. 14 Effects of dynamic pressure on the first two component modes of the aeroelastic system for the 45-deg sweptback wing at $M_\infty = 0.9$ and $\alpha_0 = 0$ deg.

mode for $Q = 0.9\ Q_{exp}$, $1.0\ Q_{exp}$, and $1.1\ Q_{exp}$, where Q_{exp} is the experimental flutter dynamic pressure value. Also shown in Fig. 13 are the two-mode curve fits of the responses, which are very good approximations to the original data. The component modes from these curve fits are shown in Fig. 14 for the three values of Q that were considered in Fig. 13. The results of Fig. 14 show that the component modes consist of a dominant mode corresponding to first bending (mode 1) and a higher-frequency damped mode corresponding to first torsion (mode 2). Also, the flutter value for Q, computed by quadratic interpolation of the damping values, was $0.92\ Q_{exp}$. Although the calculated value is slightly low in comparison with the experimental value, it is within 1% of the value predicted by the CAP-TSD transonic small-disturbance code,[16] which tends to verify the computational aeroelasticity methods of the present study.

Concluding Remarks

Modifications to the CFL3D three-dimensional unsteady Euler/Navier-Stokes code for the aeroelastic analysis of wings were described. The modifications involve including a deforming mesh capability that can move the mesh to continuously conform to the instantaneous shape of the aeroelastically deforming wing, and including the structural equations of motion for their simultaneous time integration with the governing flow equations. Calculations were performed using the Euler equations to verify the modifications to the code, and as a first step toward aeroelastic analysis using the Navier-Stokes equations.

Results were presented for the NACA 0012 airfoil and a 45-deg sweptback wing to demonstrate applications of CFL3D for generalized force computations and aeroelastic analysis. Detailed comparisons were made with published Euler results for the NACA 0012 airfoil that indicated very good agreement for generalized forces due to harmonic motion in pitch or plunge, and good agreement for aeroelastic transients corresponding to stable, neutrally stable, and unstable aeroelastic behavior. This favorable correlation tends to verify the deforming mesh capability and the aeroelastic modeling procedures that were implemented within CFL3D. Aeroelastic tran-

sients were obtained for a 45-deg sweptback wing, which also demonstrated stable, neutrally stable, and unstable behavior. The resulting flutter dynamic pressure, determined by interpolation of the dominant damping values, was within 8% of the experimental flutter value and within 1% of a transonic small-disturbance result.

Acknowledgments

The work constitutes a part of the first author's M.S. thesis at Purdue University and was supported by the NASA Langley Graduate Aeronautics Program under Grant NAG-1-372. Also, the authors would like to thank Jim Thomas and Kyle Anderson of the Analytical Methods Branch, NASA Langley Research Center, Hampton, Virginia, and Sherrie Krist of Vigyan Research Associates, Hampton, Virginia, for many fruitful discussions during the course of the present work.

References

[1]Edwards, J. W., and Thomas, J. L., "Computational Methods for Unsteady Transonic Flows," AIAA Paper 87-0107, Jan. 1987.

[2]Borland, C. J., and Rizzetta, D. P., "Nonlinear Transonic Flutter Analysis," *AIAA Journal,* Vol. 20, No. 11, 1982, pp. 1606–1615.

[3]Batina, J. T., Seidel, D. A., Bland, S. R., and Bennett, R. M., "Unsteady Transonic Flow Calculations for Realistic Aircraft Configurations," *Journal of Aircraft,* Vol. 26, No. 1, 1989, pp. 21–28.

[4]Isogai, K., and Suetsuga, K., "Numerical Simulation of Transonic Flutter of a Supercritical Wing," National Aerospace Lab., Rept. TR-276T, Tokyo, Aug. 1982.

[5]Ide, H., and Shankar, V. J., "Unsteady Full Potential Aeroelastic Computations for Flexible Configurations," AIAA Paper 87-1238, June 1987.

[6]Bendiksen, O. O., and Kousen, K. A., "Transonic Flutter Analysis Using the Euler Equations," AIAA Paper 87-0911, April 1987.

[7]Kousen, K. A., and Bendiksen, O. O., "Nonlinear Aspects of the Transonic Aeroelastic Stability Problem," AIAA Paper 88-2306, April 1988.

[8]Wu, J., Kaza, K. R. V., and Sankar, L. N., "A Technique for the Prediction of Airfoil Flutter Characteristics in Separated Flow," AIAA Paper 87-0910, April 1987.

[9]Reddy, T. S. R., Srivastava, R., and Kaza, K. R. V., "The Effects of Rotational Flow, Viscosity, Thickness, and Shape on Transonic Flutter Dip Phenomena," AIAA Paper 88-2348, April 1988.

[10]Guruswamy, G. P., "Time-Accurate Unsteady Aerodynamic and Aeroelastic Calculations of Wings Using Euler Equations," AIAA Paper 88-2281, April 1988.

[11]Rausch, R. D., Batina, J. T., and Yang, T. Y., "Euler Flutter Analysis of Airfoils Using Unstructured Dynamic Meshes," AIAA Paper 89-1384, April 1989.

[12]Anderson, W. K., Thomas, J. L., and Van Leer, B., "Comparison of Finite Volume Flux Vector Splittings for the Euler Equations," *AIAA Journal,* Vol. 24, No. 9, 1986, pp. 1453–1460.

[13]Anderson, W. K., Thomas, J. L., and Rumsey, C. L., "Extension and Application of Flux-Vector Splitting to Unsteady Calculations on Dynamic Meshes," AIAA Paper 87-1153, June 1987.

[14]Batina, J. T., "Unsteady Euler Algorithm With Unstructured Dynamic Mesh for Complex-Aircraft Aeroelastic Analysis," AIAA Paper 89-1189, April 1989.

[15]Yates, E. C., Jr., Land, N. S., and Foughner, J. T., Jr., "Measured and Calculated Subsonic and Transonic Flutter Characteristics of a 45° Sweptback Wing Planform in Air and in Freon-12 in the Langley Transonic Dynamics Tunnel," NASA TN-D-1616, March 1963.

[16]Cunningham, H. J., Batina, J. T., and Bennett, R. M., "Modern Wing Flutter Analysis by Computational Fluid Dynamics Methods," *Journal of Aircraft,* Vol. 25, No. 10, 1988, pp. 962–968.

[17]Edwards, J. W., Bennett, R. M., Whitlow, W., Jr., and Seidel, D. A., "Time-Marching Transonic Flutter Solutions Including Angle-of-Attack Effects," *Journal of Aircraft,* Vol. 20, No. 11, 1984, pp. 899–906.

[18]Edwards, J. W., Bennett, R. M., Whitlow, W., Jr., and Seidel, D. A., "Time-Marching Transonic Flutter Solutions Including Angle-of-Attack Effects," AIAA Paper 82-3685, May 1982.

[19]Bennett, R. M., and Desmarais, R. N., "Curve Fitting of Aeroelastic Transient Response Data with Exponential Functions," *Flutter Testing Techniques,* NASA SP-415, May 1975, pp. 43–58.

[20]McDevitt, J. B., and Okuno, A. F., "Static and Dynamic Pressure Measurements on a NACA 0012 Airfoil in the Ames High Reynolds Number Facility," NASA TP-2485, June 1985.

[21]Batina, J. T., "Unsteady Euler Airfoil Solutions Using Unstructured Dynamic Meshes," AIAA Paper 89-0115, Jan. 1989.

[22]Isogai, K., "Numerical Study of Transonic Flutter of a Two-Dimensional Airfoil," National Aerospace Lab., TR-617T, Tokyo, July 1980.